Received: 12 September 2024 | Revised: 7 January 2025 | Accepted: 31 January 2025

DOI: 10.1002/mrm.30468

RESEARCH ARTICLE

Magnetic Resonance in Medicine

Automated fibrosis segmentation from wideband post-contrast T_1^* mapping in an animal model of ischemic heart disease with implantable cardioverter-defibrillators

Calder D. Sheagren[1,2] | **Terenz Escartin**[1,2] | **Jaykumar H. Patel**[1,2] | **Jennifer Barry**[2] | **Graham A. Wright**[1,2]

[1]Medical Biophysics, University of Toronto, Toronto, Ontario, Canada

[2]Physical Sciences, Sunnybrook Research Institute, Toronto, Ontario, Canada

Correspondence
Calder D. Sheagren, Physical Sciences, Sunnybrook Research Institute, 2075 Bayview Avenue, Toronto, ON, M4N3M5, Canada
Email: calder.sheagren@mail.utoronto.ca

Funding information
Canadian Institutes of Health Research, Grant/Award Number: PJT-178299

Abstract

Purpose: Post-contrast T_1^* mapping has proven promising for automated scar segmentation in subjects without ICDs, but this has not been implemented in patients with ICDs. We introduce an automated cluster-based thresholding method for T_1^* maps with an ICD present and compare it to manually tuned thresholding of synthetic LGE images with an ICD present and standard LGE without an ICD present.

Methods: Seven swine received an ischemia-reperfusion myocardial infarction and were imaged at 3 T 4–5 weeks post-infarct with and without an ICD. Mapping-based thresholding was performed using synthetic LGE and artifact-corrected cluster-thresholding methods, both employing connected component filtering. Standard pixel signal intensity thresholding was performed on the conventional LGE without an ICD. Volumetric accuracy is relative to conventional LGE and Dice similarity between SynLGE and cluster-based segmentations were evaluated.

Results: No statistical significance was observed between LGE volumes without an ICD and both SynLGE and artifact-corrected cluster-threshold volumes with an ICD, when using connected component filtering. Additionally, Dice alignment between SynLGE and cluster-thresholding was high for healthy myocardium (0.96), dense scar (0.83), and dense scar union gray zone (0.91) when artifact correction and connected component filtering were implemented.

Conclusion: Clustering of T_1^* maps holds promise for a reproducible approach to scar segmentation in the presence of ICDs.

KEYWORDS

gadolinium contrast, quantitative fibrosis analysis, wideband T1 mapping

1 | INTRODUCTION

Sudden cardiac death is a leading worldwide cause of cardiac mortality.[1,2] Prevention of sudden cardiac death is now possible with the use of implantable cardiac defibrillators (ICDs), with 7 000 ICDs being implanted every year in Canada.[3] ICD therapy is not curative and only aborts acute sudden cardiac death instances, so electrophysiologic procedures such as cardiac ablations are often considered to remove the arrhythmogenic circuits and reduce ICD shocks, improving patient quality of life.[4] Pre-procedural imaging using computed tomography or magnetic resonance imaging (MRI) is an emerging method to inform electrophysiologic procedures; three-dimensional maps of dense and heterogeneous cardiac fibrosis are calculated and used to determine optimal ablation targets.[5,6] In particular, late gadolinium enhancement (LGE) MRI is often used for imaging cardiac fibrosis,[7,8] and prior work has shown that integrating LGE MRI fibrosis maps into clinical electrophysiology procedures reduces procedural time, radiation exposure to patients, and arrhythmia recurrence.[9]

While MRI has been historically contraindicated in patients with ICDs due to safety concerns, current devices are manufactured to be MRI-conditional, and large-scale studies have reported no long-term clinically significant adverse events following MRI scans in ICD patients.[10] Further, current guidelines and consensus statements endorse the use of MRI in patients with ICDs when a standardized institutional protocol including device reprogramming and patient monitoring is adhered to.[11–13] While ICDs present image quality concerns due to off-resonance artifacts from the metallic device generator, this problem has been mitigated via the integration of wideband inversion pulses that reduce hyperintensity artifacts that confound classification of healthy and injured myocardium.[14] Wideband LGE has been extensively studied in ICD patient populations and has been shown to be safe and effective in maintaining diagnostic image quality.[15–17] LGE imaging is highly sensitive to the choice of inversion time (TI) which complicates tissue classification, so post-gadolinium (Gd) T_1^* mapping has been proposed to image the myocardium at multiple inversion times and derive semi-quantitative M_0 and T_1^* maps.[18,19]

After MRI has been performed, LGE images or T_1^* maps must be segmented and post-processed to return maps depicting regions of healthy myocardium, dense scar, and heterogeneous gray zone (Figure 1). Many simple thresholding methods exist to process LGE data, but these methods require manual input to account for artifacts from coil shading, signal dropout or hyperintensity from an ICD, and changes in signal intensity histograms between magnitude and phase-sensitive LGE.[20]

While thresholding analysis of M_0 and T_1^* maps is more difficult and less agreed-upon, mapping two parameters allows for advanced segmentation methods that improve the robustness of artifacts. Prior work from Detsky et al introduced a method to calculate segmentation masks directly from the M_0 and T_1^* maps using probabilistic clustering techniques.[21] Alternatively, a simple analysis can be performed using conventional LGE thresholding techniques on intermediate synthetic LGE (SynLGE) images, which are generated using an inversion-recovery signal equation (Equation 6) with a user-specified synthetic TI (TI_{syn}) and require manual regions of interest for segmentation processing.[22,23] Both classes of methods have been evaluated without ICDs present, potentially due to the limited availability of wideband T_1 mapping techniques.[24,25] In this article, we aim to demonstrate that automated cluster-based thresholding in T_1^* maps with an ICD present agrees with manually tuned thresholding of SynLGE images generated from the same mapping data with an ICD present and agrees with thresholding of standard LGE without an ICD present.

2 | THEORY

2.1 | LGE thresholding

LGE image thresholding is most commonly accomplished with a full-width at half-maximum (FWHM) method, which has been shown to be robust and reproducible.[26,27] Specifically, two additional regions of interest are manually drawn in healthy left ventricular myocardium and dense scar. The mean signal intensities SI_{myo} and SI_{ds} are used to generate three tissue classes. Cutoff values c_{gz}, c_{ds} are defined using SI_{myo} and SI_{ds}:

$$c_{gz} := SI_{myo} + 0.5 * (SI_{ds} - SI_{myo}) = 0.5 * (SI_{myo} + SI_{ds}) \quad (1)$$

$$c_{ds} := c_{gz} + 0.5 * (SI_{ds} - c_{gz}) = 0.25 * (SI_{myo} + 3SI_{ds}). \quad (2)$$

This procedure was modified from prior work[28] for compatibility with magnitude and phase-sensitive imaging. Tissue classes

$$\text{Myo} = \{x : M(x) \leq c_{gz}\} \quad (3)$$

$$\text{GZ} = \{x : c_{gz} \leq M(x) \leq c_{ds}\} \quad (4)$$

$$\text{DS} = \{x : c_{ds} \leq M(x)\}. \quad (5)$$

were generated using the cutoff values, where Myo represents healthy myocardium, GZ represents heterogeneous

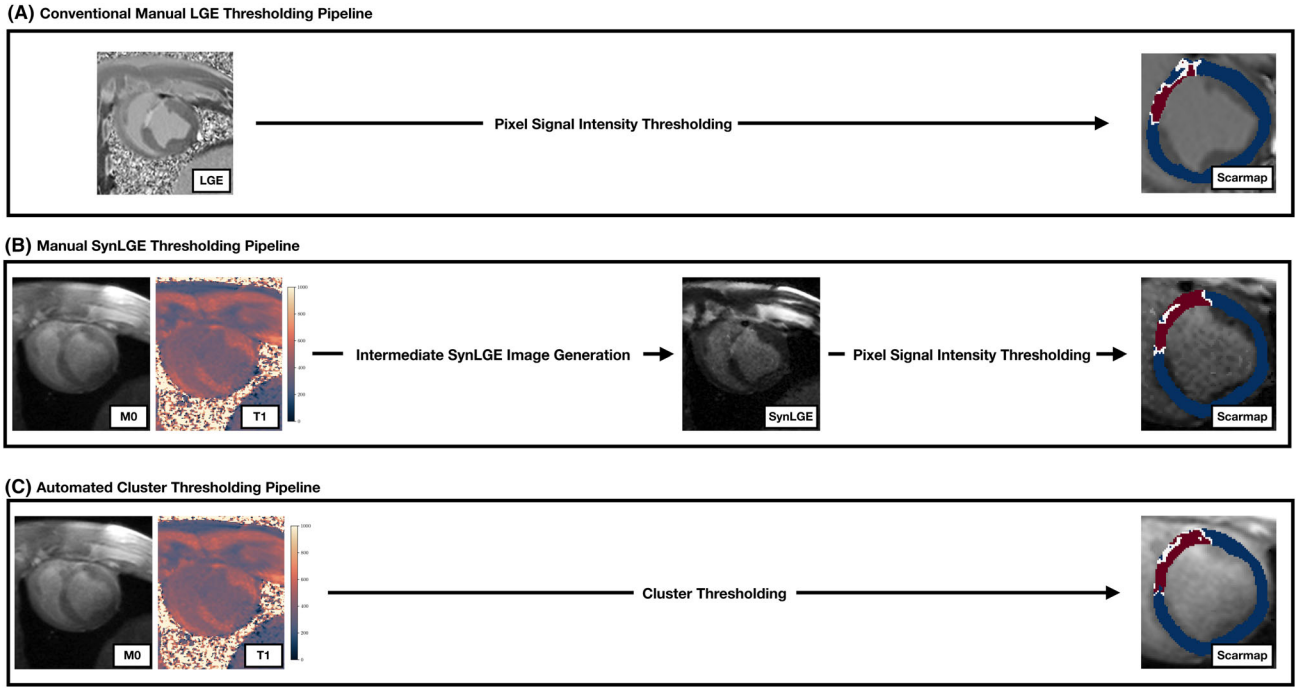

FIGURE 1 Postprocessing threshold map workflows for LGE and T_1^* mapping data, after manual epicardial and endocardial contouring. **A:** After conventional LGE images are acquired, pixel signal intensity thresholding is performed to group voxels into healthy myocardium, gray zone, and dense scar classes. This is typically performed by semi-automated thresholding methods like FWHM and NSD, but manual threshold limits can be chosen as well. **B:** M_0 and T_1^* maps can be thresholded using a similar method as in **A**, but generation of an intermediate SynLGE image is required. This intermediate SynLGE image requires a user-specified choice of retrospective TI that varies from subject to subject. **C:** Alternatively, M_0 and T_1^* maps can be thresholded using an automated method that requires no subject-specific tuning.

"gray zone" fibrosis, and DS represents dense scar. This thresholding method was used for conventional LGE without an ICD and wideband SynLGE with an ICD.

2.2 | Synthetic LGE image generation

SynLGE image generation from only post-contrast T_1 maps has been investigated in depth, where proton density is assumed to be uniform across the entire image.[22,23,29] However, these methods can break down when imaging near ICDs due to B_0 and B_1 variations near the heart.[30] As such, in this method, we perform a retrospective M_0 and T_1^* fit using a two-parameter signal equation

$$M(\mathrm{TI}) = M_0\left(1 - 2\exp\left(-\mathrm{TI}/T_1^*\right)\right) \tag{6}$$

and use both of these maps to generate SynLGE images that are more robust to off-resonance artifacts. Data was normalized to a consistent range of [0, 1] for fitting and was not divided by the proton density term to improve computation time and limit divide-by-zero errors.

Manual left ventricular segmentation was performed on the M_0 images due to the improved blood-scar contrast, in regions of septal tissue to avoid regions of off-resonance artifact. An optimal $\mathrm{TI}_{\mathrm{syn}}$ was manually selected to null healthy myocardium and maximize contrast between healthy myocardium and dense scar (Supporting Information in Figure S1). After image generation, SynLGE images were thresholded using the same procedure as the clinical LGE images.

2.3 | Cluster-thresholding

Cluster-thresholding automatically generates healthy myocardium, gray zone, and dense scar maps from M_0, T_1^* maps in left ventricular tissue without generating auxiliary LGE volumes. This method was proposed by Detsky et al.[21] and is applied here with changes to the core algorithm, postprocessing, and filtering to account for the presence of ICDs. The main mathematical tool for these calculations is fuzzy clustering, which generates probabilistic segmentation maps

$$P_c(x) = P\left(\left(M_0(x), T_1^*(x)\right) \in \text{cluster } c\right), \tag{7}$$

for $c = 1, \ldots, N_{\mathrm{center}}$. Conventional fuzzy clustering uses three cluster centers to identify healthy myocardium, dense scar, and left ventricular blood from a region of

interest drawn within a single epicardial contour. Specifically, a voxel x within the manually segmented myocardium is assigned to the cluster corresponding to the maximum probability at that point. The gray zone mask is determined by selecting voxels with a marginal probability of at least $GZ_{cut} = 25\%$ for both healthy myocardium and dense scar. Finally, a four-class map is generated by removing gray zone voxels from healthy myocardium and dense scar segmentation maps.

In this work, endocardial and epicardial contouring are both performed, and two cluster centers are used to identify healthy myocardium and dense scar. Gray zone identification is identical to prior work; Supporting Information in Figure S2 shows the influence of the GZ_{cut} value on threshold maps, when compared to standard LGE thresholding. A three-class map is generated in a similar manner, identifying voxels as healthy myocardium, gray zone, or dense scar.

2.4 | Cluster-based artifact removal

Cluster-thresholding in the presence of ICDs requires special consideration due to artifacts from incoherent dephasing, incomplete inversion, and residual off-resonance (Figure 2). In particular, regions of high susceptibility gradient interact with the incremental increase in off-resonance due to the ICD to artifactually reduce M_0 and T_1^*. Without correction, these regions of signal loss artifacts in the inferolateral wall appear as fibrosis in the cluster-based threshold maps, degrading scarmap quality. To correct for this in an automated fashion, we first perform a fuzzy clustering calculation with three cluster centers using M_0, T_1^* data that are separately normalized to a signal intensity range of $[0, 1]$. The cluster with the lowest mean M_0 value was selected as the artifact cluster and used to generate a spatial artifact mask.

After creating the artifact mask, a standard fuzzy clustering calculation is performed as described in Section 2.3. The artifact mask is propagated onto the segmentation results, and tissue in the artifact mask is set to healthy myocardium. Figure 3 shows the effect of artifact correction on cluster-thresholding data and its interaction with connected component filtering.

2.5 | Connected component filtering

A final step used in all thresholding calculations is connected component filtering. Inspired by more complex normalized cut filtering methods, this procedure is used to remove spurious regions of artifactual gray zone or dense scar due to statistical noise or mis-contoured blood pool voxels.[31]

For this procedure, voxels classified as either dense scar or gray zone were temporarily assigned a pixel value of "1", and all other voxels classified as healthy myocardium were assigned a pixel value of "0". Pixel values of "1" were grouped by connected component, and the connected component with the largest pixel count was assumed to

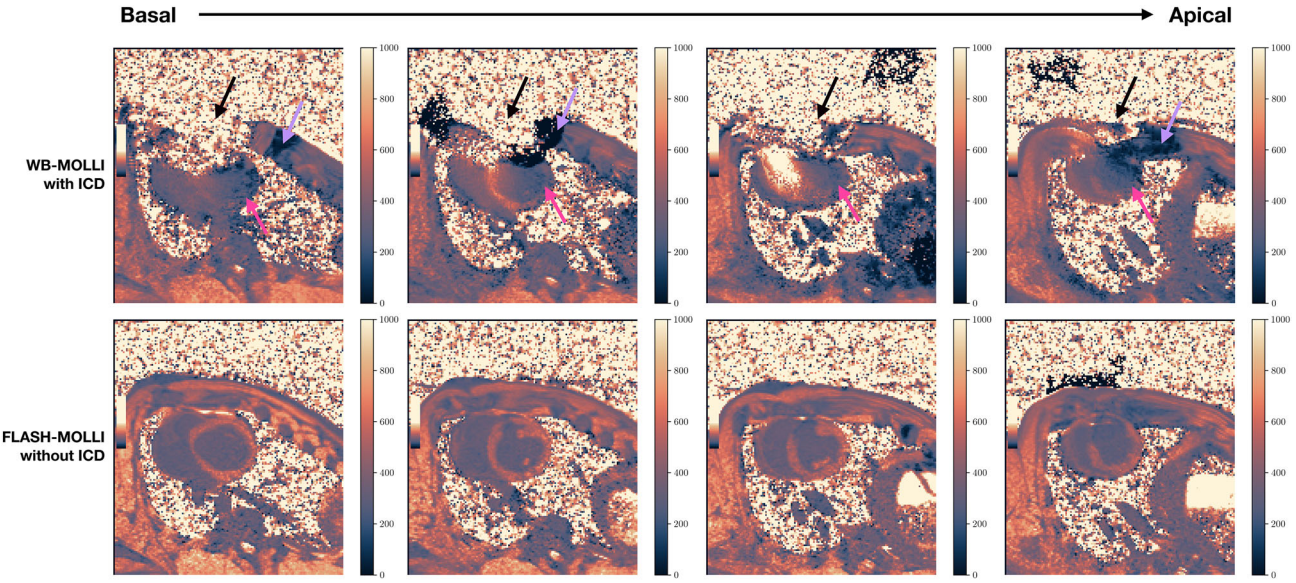

FIGURE 2 Characterization of artifacts due to ICD on WB-MOLLI data, shown in vendor T_1 map reconstructions of separate mapping data not used for fibrosis mapping. Top row: WB-MOLLI with an ICD. Bottom row: FLASH-MOLLI without an ICD. Black arrows indicate regions of incoherent dephasing. Purple arrows indicate regions of incomplete inversion. Magenta arrows indicate regions of T_1 hypointensity from residual off-resonance. Yellow arrows indicate regions of true fibrosis, some of which are obscured by ICD artifacts.

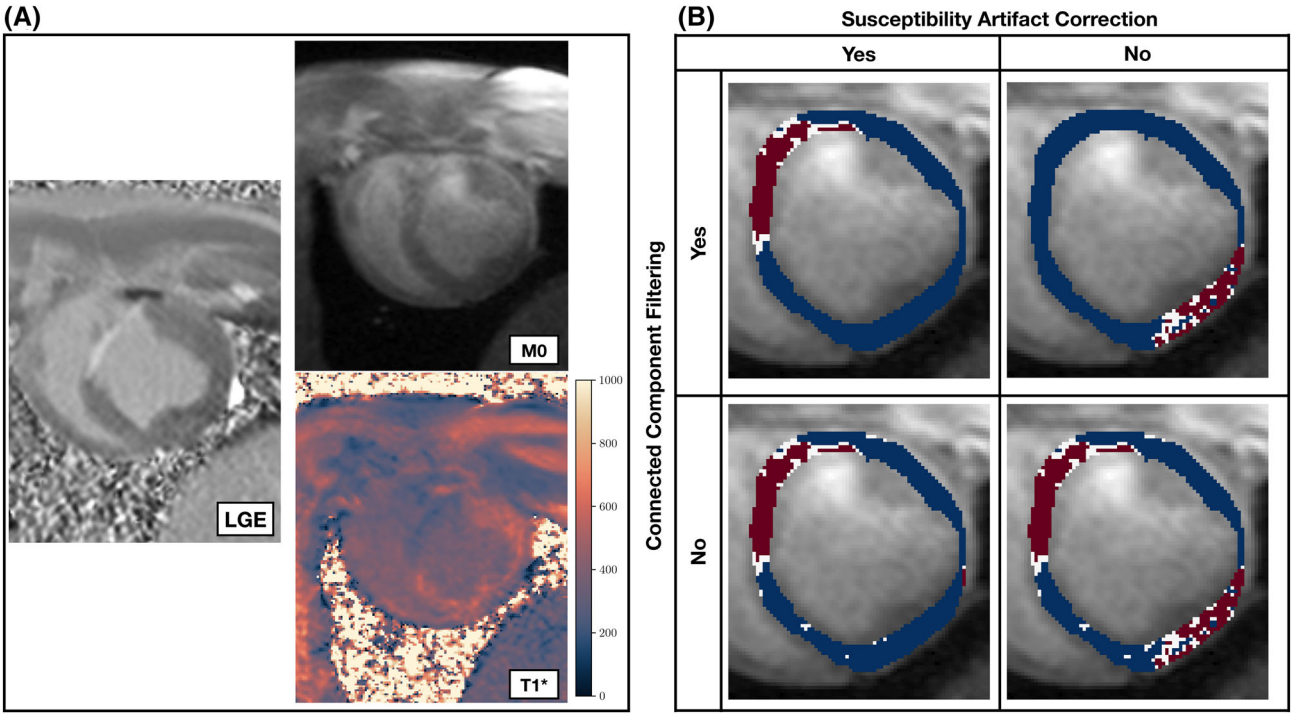

FIGURE 3 Susceptibility artifact correction and connected component filtering. **A:** Reference LGE image with M_0 and T_1^* data. **B:** Cluster-thresholding maps with different post-processing strategies. Susceptibility artifact correction ensures that regions of spurious enhancement due to artifactually low T_1^* values are suppressed, improving fibrosis localization with reference LGE. Connected component filtering reduces the contribution of statistical noise and mis-contoured blood pool voxels to the enhancement pattern. Usage of connected component filtering without artifact correction results in scarmaps with incorrect fibrosis location.

be the physiological region of infarcted tissue, with pixels outside this region being set to "0". Finally, pixels with the value "0" were reassigned to healthy myocardium in the final tissue maps. In this paper, 3D connected component filtering followed by 2D connected component filtering is used to remove spurious regions of enhancement. Figure 3 demonstrates the effect of connected component filtering and its interaction with artifact correction in cluster-thresholding data.

3 | METHODS

3.1 | Animal model and data acquisition

7 swine (5 male, nominal weight: 60 kg at the time of imaging) were studied; all procedures were approved by the Sunnybrook Animal Care Committee. Swine received an ischemia-reperfusion myocardial infarction via a 100-min balloon occlusion of the left anterior descending coronary artery. Animals were scanned 4–5 weeks post-infarct with a 2D multi-slice prototype wideband motion-corrected FLASH-MOLLI (WB-MOLLI) T_1 mapping sequence with an ICD (Cognis 100-D, Boston Scientific, Marlborough MA, USA) present and conventional 2D multislice phase-sensitive LGE imaging without the ICD present. The ICD was taped on the pigs' chest approximately 8–12 cm away from the heart to mimic the artifacts seen in patients. All scans were performed on a 3 T PET-MRI scanner (Biograph mMR, Siemens Healthcare AG, Erlangen, Germany). Sequence parameters for WB-MOLLI include: Scan time = 9 heartbeats per slice, field of view = 280×252 mm^2, phase oversampling = 50%, partial Fourier = 6/8, slice thickness = 5 mm, resolution = 1.8×1.8 mm^2, TR/TE/flip angle = 5.1 ms/2.78 ms/12°, TI = [100, 100 + RR, 100 + 2RR, 100 + 3RR, 180, 180 + RR, 180 + 2RR, 260, 260 + RR] ms, linear phase-encode ordering, no asymmetric echo. TIs were updated in cases of cardiac mistriggering to reflect the observed trigger delays. No asymmetric echo was used for WB-MOLLI despite the longer TE to maintain adequate SNR in the multi-contrast T1w images. A 4(1)3(1)2 acquisition scheme was used for measurement of post-contrast T_1 values[32]; a sequence diagram is shown in Supporting Information in Figure S3. A 4 kHz adiabatic hyperbolic secant inversion pulse was used in WB-MOLLI to suppress ICD artifacts. Non-rigid motion correction was utilized to correct inter-shot motion arising from cardiac mistriggering and respiratory drift.[33] Sequence parameters for conventional phase-sensitive LGE include scan time = 14 heartbeats per slice, field of

view = 350×263 mm^2, slice thickness = 5 mm, phase oversampling = 0%, partial Fourier = 8/8, resolution = 1.6×1.6 mm^2, TR/TE/flip angle = 4.1 ms/1.64 ms/20°, TI = [220, 300] ms depending on time since Gd injection, linear phase-encode ordering, weak asymmetric echo. A conventional adiabatic inversion pulse was used.

In 5 animals, phase-sensitive LGE was performed 5 min after Gd injection with a nominal TI = 220 ms, and WB-MOLLI was performed 20 min after Gd injection. In the other two animals, WB-MOLLI was performed 5 min after Gd injection and phase-sensitive LGE was performed 20 min after Gd injection, with a nominal TI = 300 ms. WB-MOLLI TIs were not changed between the two cases.

3.2 | Image processing

Conventional PSIR-LGE without an ICD and M_0 images from the T_1^* fitting with an ICD were contoured in ITK-Snap,[34] where a myocardium segmentation mask was manually generated using the paint tool. All left ventricular slices were contoured for PSIR-LGE, and all left ventricular slices with no incomplete dephasing or incomplete inversion artifacts were contoured in the WB-MOLLI dataset. Additional regions of interest were drawn in healthy and infarcted myocardium for PSIR-LGE and WB-MOLLI separately as an input to the FWHM thresholding as discussed in Section 2.1.

T_1^* fitting and SynLGE image generation was performed using the SyntheticLGE.jl toolkit.[30] SynLGE thresholding was performed on generated LGE images, and artifact-corrected cluster-thresholding was performed on multi-contrast images using a python-based fuzzy clustering program.[35] FWHM thresholding was performed on the clinical PSIR dataset using custom Python code. All volume maps were post-processed using connected component filtering; connected component identification was performed using the `measure.label()` function from Scikit-Image.[36]

3.3 | Experiments and statistical analysis

The hypothesis of this paper is that automated cluster-thresholding has non-inferior fibrosis volumetric accuracy to manually optimized SynLGE-based fibrosis volumetric accuracy in the same T_1^* mapping dataset, when compared to conventional LGE. Further, automated cluster threshold maps will be spatially aligned to optimized SynLGE threshold maps. Together, these hypotheses demonstrate that accurate and aligned scarmaps can be generated from T_1^* mapping data with an ICD present, with limited operator input. This hypothesis was tested using two metrics: Volumetric accuracy with LGE without an ICD as the reference standard, and spatial alignment using Dice similarity between SynLGE and cluster-based segmentations on the same underlying mapping data. A two-tailed independent-samples *t*-test was used to determine the significance between tissue volumes, and a one-way ANOVA with post-hoc Tukey test was used to assess statistical differences between distributions of Dice coefficients.

4 | RESULTS

T_1^* mapping and SynLGE image generation were successfully implemented in Julia, and pixel signal intensity thresholding and cluster-thresholding were successfully implemented in Python. For a single volume, T_1^* mapping required 49 s of compute time, SynLGE image generation required 0.05 s of compute time, pixel signal intensity thresholding required 0.66 s of compute time, and cluster-thresholding required 1.37 s of compute time, with a maximum RAM usage of 7.3GB for T_1^* mapping and 4.2GB for thresholding on a workstation laptop with a 12-core intel i7-9750H CPU with 32GB RAM. The largest computation time is needed for T_1^* mapping, with cluster-thresholding requiring approximately twice as long as pixel signal intensity thresholding.

Figure 4 demonstrates the thresholding process in the presence of ICD artifacts. Notably, a signal dropout occurs in M_0 maps, which propagates to SynLGE images, and several types of artifacts occur in T_1 or T_1^* maps, as shown in Figure 2. Briefly, incoherent dephasing artifacts cause a loss of spatial T_1 information in a region close to the ICD (black arrows in Figure 2); incomplete inversion artifacts cause a reduction in T_1 in the periphery of the incoherent dephasing artifact caused by the spins not being inverted (purple arrows); and residual off-resonance artifacts cause reductions in T_1 further from the device in regions of large magnetic susceptibility gradients due to the increased off-resonance from the ICD (magenta arrows). Regions of true fibrosis (yellow arrows) can be obscured by the ICD, causing the computed scar volume to be larger than arising from the off-resonance artifact. As a remark, changes in T_1 solely due to the wideband pulse can be thought of as negligible-several previous studies demonstrate good agreement between conventional and wideband mapping techniques without ICD artifacts present, with no statistically significant differences[24,25,37]

Figure 5 demonstrates sample curve fits for regions of interest drawn in healthy myocardium, dense scar, and artifact. Regions of artifact contain lower SNR in T_1w

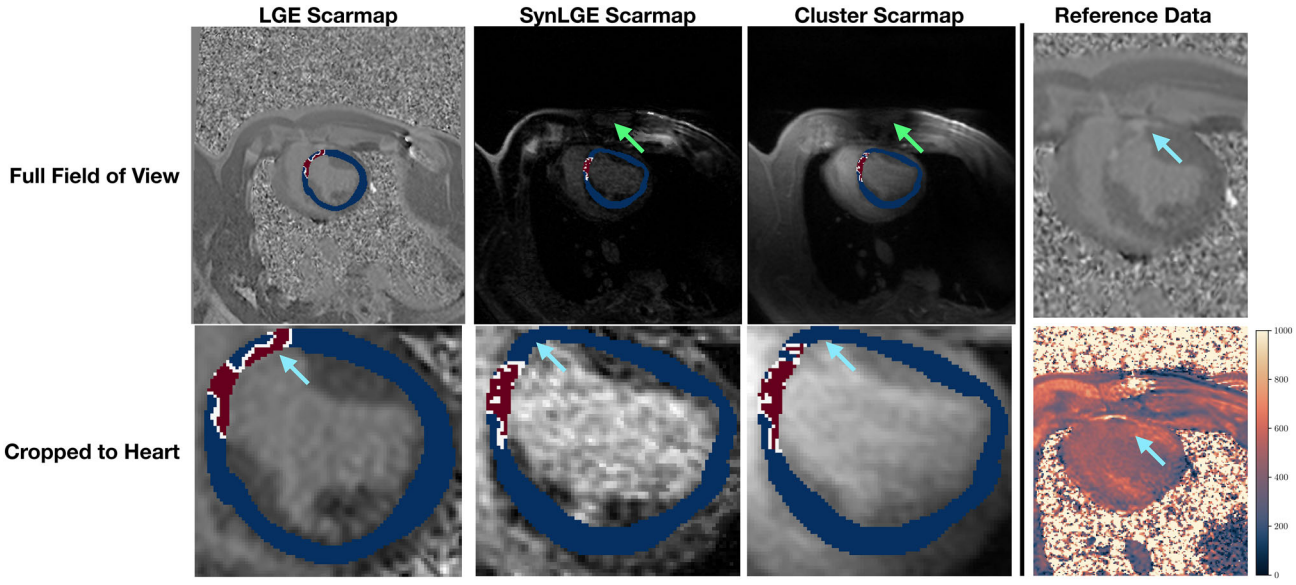

FIGURE 4 Sample scarmaps in slices with visible ICD artifact in mapping-based data. Top row: Full field of view images. Bottom row: Images cropped to the heart. Right column: Reference LGE image and T1 map without thresholds. The green arrow indicates regions of signal loss due to the ICD that is disjoint from the heart. Teal arrows indicate a missing region of fibrosis in the anterior wall adjacent to a region of microvascular obstruction seen in the conventional LGE scarmap.

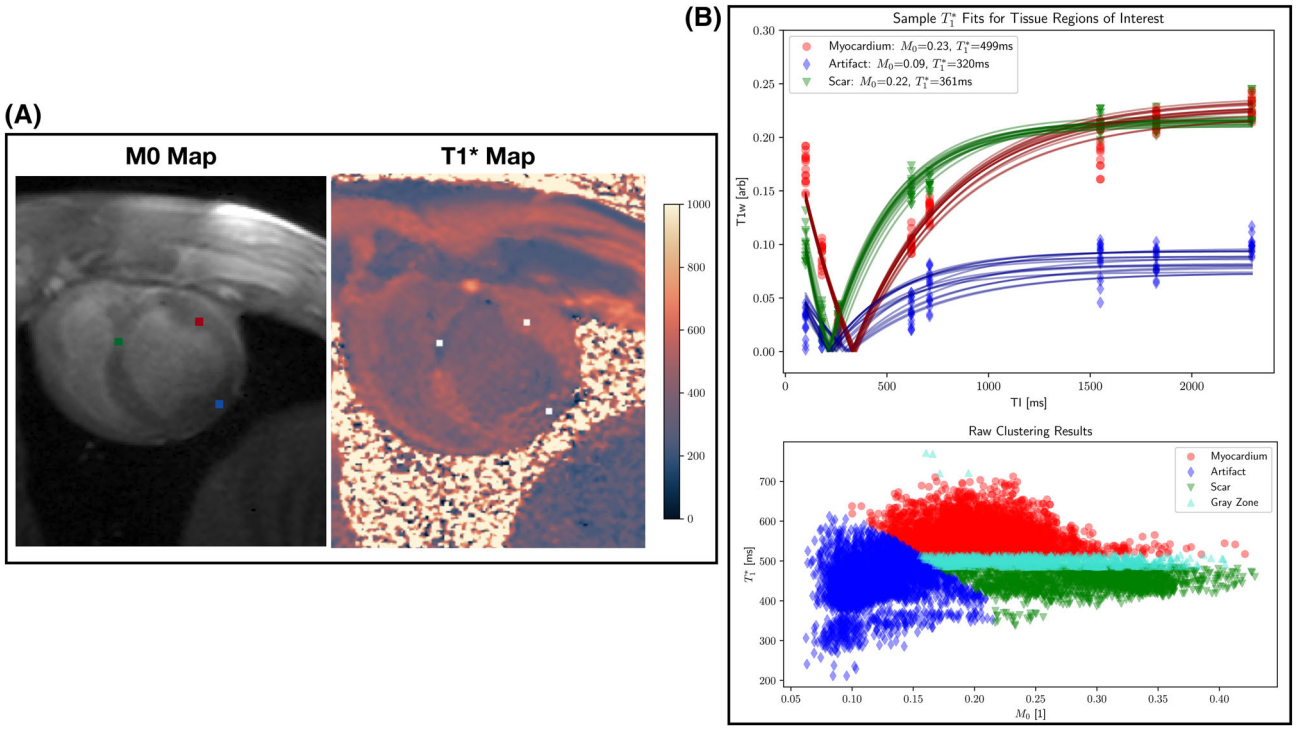

FIGURE 5 Sample M_0 and T_1^* curve fits and cluster-maps. **A:** M_0 and T_1^* maps are annotated with three regions of interest: Red in healthy myocardium, blue in artifact, and green in dense scar. **B:** Top row: Sample curve fits are shown for voxels within the regions of interest. In particular, low M_0 SNR in the artifact cluster causes an artifactual decrease in T_1^*. Bottom row: Clustering results show the (M_0, T_1^*) pairs, classified into tissue types. The boundary separating the artifact region from the myocardium, gray zone, and dense scar regions is dependent on both M_0 and T_1^*, whereas the gray zone boundary between myocardium and the dense scar is largely invariant of M_0.

images, causing an artificial reduction in T_1^*. Additionally, sample clustering results are shown: The boundary separating artifact from non-artifact is dependent on both M_0 and T_1^*, but the gray zone boundary between healthy myocardium and the dense scar is largely independent of M_0.

Figures 6 and 7 demonstrate sample threshold maps in two representative animals. In Figure 6, SynLGE and cluster-thresholding scars have a similar enhancement pattern to LGE without an ICD. In Figure 7, cluster-thresholding demonstrates less artificial enhancement than SynLGE or conventional LGE, where no fibrosis is present and a substantial ICD artifact obscures the myocardium.

No significant volumetric differences were observed for myocardium, dense scar, and dense scar union gray zone between any T_1^* mapping-based technique with an ICD present and LGE without an ICD, when connected component filtering was applied (Table 1). Gray zone volumes were only significantly different from LGE without an ICD for cluster-thresholding without artifact correction, which overestimated the mean gray zone by nearly a factor of two. Without connected component filtering (Table S1), all SynLGE volumes with an

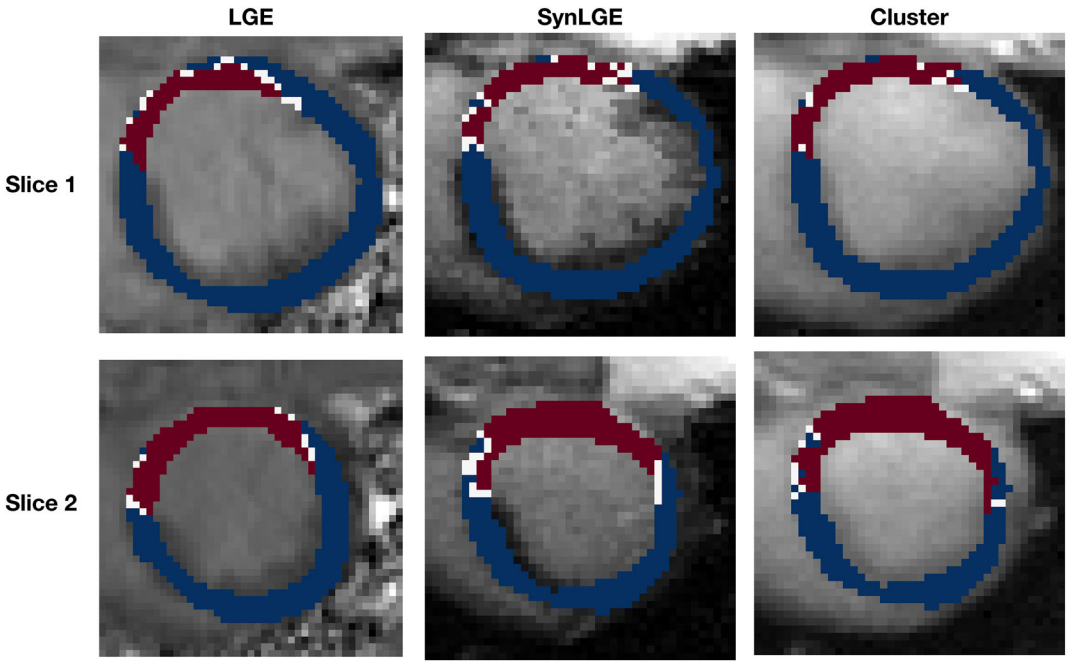

FIGURE 6 Sample threshold maps from two adjacent slices in one representative animal. Left column: Conventional LGE threshold maps. Center column: SynLGE threshold maps. Right column: Cluster-threshold maps overplotted on the fitted M_0 map.

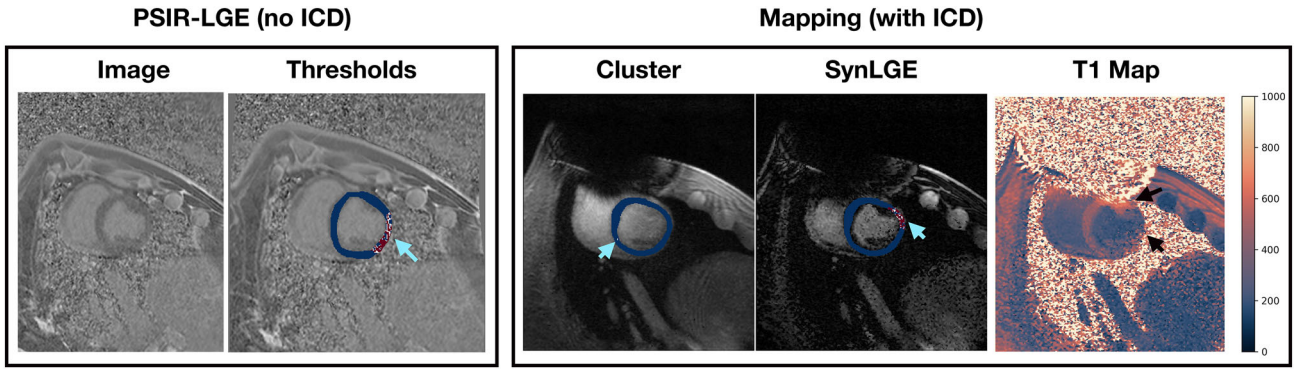

FIGURE 7 Performance of automated clustering in an animal not included for quantitative analysis with substantial ICD artifact. The presented slice has no fibrosis, so any enhancement in scarmaps is artifactual. Left block: PSIR-LGE thresholding demonstrates artifactual enhancement due to the presence of noise. Right block: SynLGE demonstrates artifactual hyperenhancement in the lateral wall due to residual off-resonance artifact, whereas cluster thresholding has greatly reduced artifactual enhancement, with small gray zone enhancement and no dense scar region.

TABLE 1 Volumetric results for T_1^* mapping-based scarmaps with an ICD present and LGE scarmaps without an ICD present with all techniques using connected component filtering.

Volumes [mL]	Clinical LGE	SynLGE	Cluster	AC + Cluster
Myocardium	6.23 ± 7.85	7.16 ± 8.53, p = NS	8.10 ± 8.03, p = NS	8.19 ± 8.88, p = NS
Gray Zone	0.45 ± 0.60	0.35 ± 0.46, p = NS	0.82 ± 1.07, $p < 0.05$	0.51 ± 0.73, p = NS
Dense Scar	3.59 ± 6.90	4.04 ± 7.13, p = NS	2.64 ± 2.79, p = NS	2.85 ± 4.78, p = NS
Union	4.04 ± 6.86	4.39 ± 7.09, p = NS	3.46 ± 3.64, p = NS	3.37 ± 4.87, p = NS

Note: Cluster: *Cluster-thresholding*; AC: *Artifact correction*; Union: *Dense scar union gray zone*.

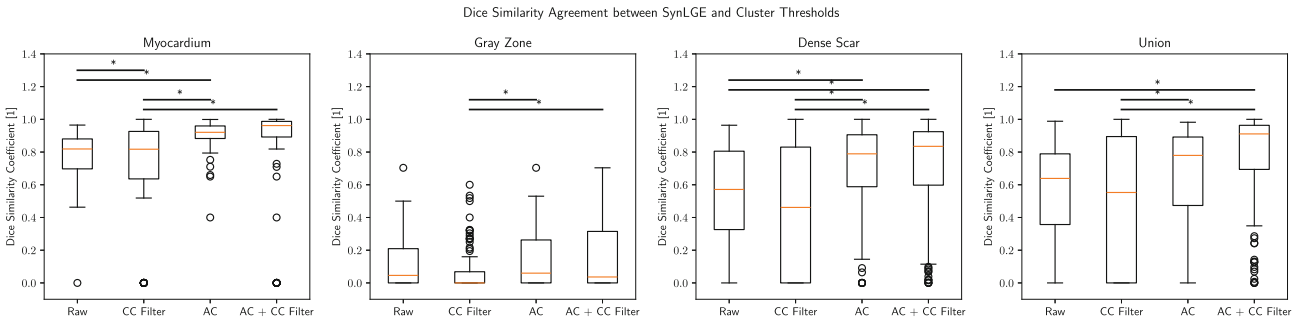

FIGURE 8 Dice similarity between SynLGE and cluster-thresholding scarmaps generated from the same underlying data. Artifact correction and connected component filtering return the highest median Dice similarity for myocardium, dense scar, and dense scar union gray zone. Artifact correction without connected component filtering returns the highest Dice similarity in the gray zone, which may be due to the loss of spurious gray zone regions in the connected component filtering process. CC filter: *Connected component filtering*; AC: *Artifact correction*; Union: *Dense scar union gray zone*.

ICD remain not statistically significantly different than the same volumes from conventional LGE without an ICD, but most cluster-thresholding and artifact-corrected cluster-thresholding volumes were significantly distinct from LGE without an ICD. As such, we can conclude that volumetric accuracy is acceptable for artifact-corrected cluster-thresholding and SynLGE, but such measures are an incomplete measure of success, as the volumetric agreement does not imply spatial co-localization.

Dice similarity was evaluated between T_1^* mapping-based thresholding methods with an ICD present, with SynLGE as the reference standard (Figure 8). Dice similarity between mapping-based methods and conventional LGE is not shown here due to the need for image registration because of the mismatched field of view and matrix size. Combining artifact correction and connected component filtering results in the highest median Dice similarity for myocardium (0.96), dense scar (0.83), and dense scar union gray zone (0.91). However, the Dice distribution of artifact-corrected cluster-thresholding is not significantly different from that of artifact-corrected cluster-thresholding with connected component filtering for these tissue types. For the gray zone, artifact correction without connected component filtering returned the highest median Dice value (0.06 vs. 0.04), but this is not statistically significant. In general, gray zone Dice is lower than other tissue types due to the differing criteria for assigning gray zone voxels.

5 | DISCUSSION

5.1 | Main findings

In this article, an automated cluster-thresholding method for fibrosis quantification from wideband T_1^* mapping with an ICD present was evaluated and compared to SynLGE thresholding from the same data with an ICD and conventional LGE without an ICD. The automated clustering pipeline requires no manual intervention, whereas SynLGE requires a manual choice of TI_{syn} and manual regions of interest. Cluster-threshold scarmaps look visually similar to SynLGE scarmaps from the same dataset with an ICD present and are spatially localized with the territory of enhancement in conventional LGE without an ICD. No statistical significance was observed between LGE volumes without an ICD and both SynLGE and artifact-corrected cluster-threshold volumes with an ICD, when using connected component filtering. However, significant volumetric differences were noted in gray zone

volume with non-corrected cluster-thresholding data, indicating the need for artifact suppression. Additionally, Dice alignment between SynLGE and cluster-thresholding was high for healthy myocardium (0.96), dense scar (0.83), and dense scar union gray zone (0.91) when artifact correction and connected component filtering were implemented. The dice similarity of the gray zone is lower, which we hypothesize is due to the varying criteria for gray zone assignment.

Cluster-based artifact correction is essential to ensure spatial localization of fibrosis enhancement with LGE, as large regions of spurious enhancement are in a different territory than the infarct in this work. With or without connected component filtering, artifact correction specifically removes low-T_1^* voxels that also have low M_0 that indicates low SNR values in the T_1w images. The low SNR in the inferolateral wall is a result of increased off-resonance in an area of already high susceptibility gradients (Figure 2). A simple SNR cutoff for artifact detection may be sufficient for determining a large enough region to remove for the connected component filtering to clean up, but this introduces another manual parameter, whereas the cluster-based correction is fully automatic. The rationale for connected component filtering arises from physiological arguments that dense and heterogeneous fibrosis forms a single connected component in ischemic infarcts. While connected component filtering is intended to remove small areas of spurious enhancement, larger areas of physiological infarct can be removed when artifact correction is not used if the region of spurious enhancement has a larger volume than the physiological infarct.

When comparing wideband motion-corrected T_1^* mapping with state-of-the-art wideband motion-corrected LGE techniques,[38–40] several similarities and differences are present. In WB-MOLLI, one TI is acquired per heartbeat, which has the potential for misregistration between TIs. However, motion correction improves alignment across TIs, which reduces misregistration-induced T_1^* error. In comparison to wideband LGE, wideband T_1^* mapping singular images have reduced SNR and respiratory motion compensation performance due to the lack of repeated single-contrast acquisitions. Notably, wideband LGE is robust to free-breathing acquisitions, whereas motion-compensated wideband T_1^* mapping is only robust to residual respiratory motion within a breath-hold.[33] However, the implementation of motion correction into the T_1^* mapping pipeline improves robustness to respiratory drift and cardiac mistriggering seen in our animal model.[41] Additionally, wideband T_1^* mapping allows for the analysis of two separate parameters that allow for the decoupling of spatial proton density from physiological signal recovery.

5.2 | Limitations

This article acknowledges several limitations that are worth discussing. First, while T_1^* mapping techniques are more robust to individual TI choice than LGE, there is still a dependence on the time since Gd injection. Since T_1 and T_1^* values change over time since Gd injection, the choice of TIs used in the mapping sequence will need to reflect the expected T_1 values at the desired time since injection. Notably, changing the time since injection will require modification of the sequence TIs for optimal results. Notably, the T_1 maps acquired at 5 min post-Gd were of lower quality due to the limited sampling at short inversion times needed to accurately characterize T_1 shortly after Gd injection.

The artifact correction method in this method largely identifies the region of low M_0 on the inferolateral wall, which is consistent with prior work using dedicated off-resonance mapping.[42] However, performing artifact correction using M_0 and T_1^* directly, instead of performing dedicated B_0 measurements, limits the method's robustness in regions of inferior infarcts. While performance is reasonable in left anterior descending-territory infarcts presented here that do not generally overlap with this region of off-resonance, future work will need to consider the interaction between true infarct and off-resonance for generalization to multiple territories.

Manual epicardial and endocardial contours are required for all thresholding methods presented in this work, which may introduce interobserver bias. The connected component filtering partially mitigates this, but does not edit the largest regions of fibrosis, where endocardial contours may include blood pool signal that ends up misclassified as fibrosis. While cluster-thresholding avoids the need for manual regions of interest or manually selected TI_{syn}values, contouring is still performed manually, and implementing an automated myocardial segmentation step would allow for fully automated post-processing.

Our animal model with an ICD only used an externally taped device, with no leads present. While the generator artifact is similar to what is seen in humans, ICD leads create small artifacts in the right ventricular blood pool or septum, which may need to be taken into account in future studies. Additionally, the infarct patterns seen in pigs have been allowed to mature for 4–5 weeks, which does not allow for the modeling of more complex pathologies such as concurrent non-ischemic cardiomyopathy and intramyocardial fat. Human anatomy is also different from porcine anatomy, with a less pronounced heart-lung interface; this will likely decrease the T_1 hypointensity artifact size compared to our data in porcine scans. Finally, this

study is performed at 3 T, which is not the clinical standard field strength for ICD patient scans. As such, incoherent dephasing and T_1 hypointensity artifact volumes are expected to be less at 1.5 T due to the decreased susceptibility gradient between lung air and myocardial tissue.

5.3 | Future directions

Technical developments in the mapping sequence and analysis can improve the performance and robustness of the techniques introduced in this paper. First, this work uses Cartesian sampling, which is generally robust to off-resonance artifacts, but not robust to intra-shot motion, so the use of a non-Cartesian sampling pattern may allow for improved motion robustness in patients with unstable heart rhythms. Recent work uses a 2D golden-angle radial readout and a modified GRASP-Pro reconstruction to generate motion-robust single-shot multi-TI LGE images that are inherently robust to arrhythmia.[43] Additionally, decreasing the temporal resolution of each single-shot image improves motion robustness during periods of abnormal rapid contraction, as seen in arrhythmias, but requires advances in image reconstruction to account for the reduction in *k*-space lines.[44] As an alternative, segmented multi-contrast late enhancement acquisitions have been proposed to acquire multiple sub-bins within cardiac diastole.[45] However, motion compensation would be needed to successfully implement segmented methods in patients with arrhythmias due to the need for combining data across multiple heartbeats: Recent work demonstrates the potential for robust motion compensation using a deep learning-based groupwise registration technique.[46] As well, 3D T_1^* mapping would allow for improved inter-slice alignment as well as the potential for higher spatial resolution to identify smaller regions of arrhythmogenic tissue. The thresholding techniques used in this paper only require co-registered M_0 and T_1^* maps, so other mapping sequences can be used, such as SASHA,[47] AIR T_1 mapping,[24] or MR Fingerprinting.[48]

All thresholding methods in this article require manual myocardial segmentations, which introduce uncertainty and add manual processing steps. Integration of deep learning-based myocardial segmentation would allow for fully automated and reproducible analysis.[31,49] As well, deep learning-based dense and heterogeneous infarct segmentation has been proposed using LGE images[50] and may provide incremental accuracy improvements to statistical learning methods presented in this paper. However, deep learning-based methods require a large training dataset and have optimal performance only on data similar to that it has been trained on, limiting generalizability to datasets with patient-specific ICD artifacts. Finally, the spatial analysis in this work uses connected component analysis, which is a low-order topological feature. Integration of higher-order topological features may improve specificity to arrhythmia substrate.[51,52]

6 | CONCLUSION

In conclusion, an automated cluster-thresholding method for fibrosis quantification from wideband T_1^* mapping with an ICD present was evaluated and compared to SynLGE thresholding from the same data with an ICD and conventional LGE without an ICD. In the current study, cluster-based thresholding demonstrates non-inferior performance to SynLGE, which requires manual TI_{syn} selection and regions of interest for accurate segmentation calculations. Future work aims to improve the robustness of the sequence and analysis of artifacts from physiological motion and off-resonance.

ACKNOWLEDGMENTS

The authors would like to thank Melissa Larsen for help with animal care, Brandon Tran and Dr. Angus Lau for their help in developing the SyntheticLGE.jl software, and Dr. Eranga Ukwatta for helpful discussions on this work. The source code for motion-compensated MOLLI and wideband inversion pulses was provided by Siemens Healthineers.

CONFLICTS OF INTEREST STATEMENT

GAW receives research support from GE Healthcare and Vista AI as well as non-monetary research support from Siemens Healthineers. Other authors report no conflicts of interest.

ORCID

Calder D. Sheagren https://orcid.org/0000-0001-7439-2906

Jaykumar H. Patel https://orcid.org/0000-0003-1954-4879

REFERENCES

1. Martinez-Rubio A, Bayes-Genis A, Guindo J, Luna A. Sudden cardiac death. *Contributions to Science, ISSN 1575-6343*. 1999;1:147-157.
2. Zheng ZJ, Croft JB, Giles WH, Mensah GA. Sudden cardiac death in the United States, 1989 to 1998. *Circulation*. 2001;104:2158-2163.
3. Kelly SE, Debra C, Duhn LJ, et al. Remote monitoring of cardiovascular implantable electronic devices in Canada: survey of patients and device health care professionals. *CJC Open*. 2021;3:391-399.
4. Reddy VY, Reynolds MR, Neuzil P, et al. Prophylactic catheter ablation for the prevention of defibrillator therapy. *N Engl J Med*. 2007;357:2657-2665.

5. Roca-Luque I, Mont-Girbau L. Cardiac magnetic resonance for ventricular tachycardia ablation and risk stratification. *Front Cardiovasc Med.* 2022;8:797864. doi:10.3389/fcvm.2021.797864
6. Berruezo A, Penela D, Jáuregui B, et al. Twenty-five years of research in cardiac imaging in electrophysiology procedures for atrial and ventricular arrhythmias. *EP Europace.* 2023;25:euad183.
7. Kim RJ, Wu E, Allen R, et al. The use of contrast-enhanced magnetic resonance imaging to identify reversible myocardial dysfunction. *N Engl J Med.* 2000;343:1445-1453.
8. Andreu D, Ortiz-Perez JT, Fernandez-Armenta J, et al. 3D delayed-enhanced magnetic resonance sequences improve Conducting Channel delineation prior to ventricular tachycardia ablation. *EP Europace.* 2015;17:938-945.
9. Soto-Iglesias D, Penela D, Jauregui B, et al. *Cardiac Magnetic Resonance-Guided Ventricular Tachycardia Substrate Ablation*. Vol 6. Clinical Electrophysiology; 2020:436-447.
10. Nazarian S, Hansford R, Rahsepar AA, et al. Safety of magnetic resonance imaging in patients with cardiac devices. *N Engl J Med.* 2017;377:2555-2564.
11. Bhuva A, Charles-Edwards G, Ashmore J, et al. Joint British society consensus recommendations for magnetic resonance imaging for patients with cardiac implantable electronic devices. *Heart.* 2022;110:e3.
12. Paterson DA, White JA, Butler CR, et al. 2021 update on safety of magnetic resonance imaging: Joint statement from Canadian cardiovascular society/Canadian Society for Cardiovascular Magnetic Resonance/Canadian Heart Rhythm Society. *Can J Cardiol.* 2021;37:835-847.
13. Kim D, Collins JD, White JA, et al. SCMR expert consensus statement for cardiovascular magnetic resonance of patients with a cardiac implantable electronic device. *J Cardiovasc Magn Reson*. 2024;26:100995.
14. Rashid S, Rapacchi S, Marmar V, et al. Improved late gadolinium enhancement MR imaging for patients with implanted cardiac devices. *Radiology.* 2014;270:269-274.
15. Rashid S, Rapacchi S, Shivkumar K, Plotnik A, Finn JP, Hu P. Modified wideband three-dimensional late gadolinium enhancement MRI for patients with implantable cardiac devices. *Magn Reson Med.* 2016;75:572-584.
16. Roca-Luque I, Van Breukelen A, Alarcon F, et al. Ventricular scar channel entrances identified by new wideband cardiac magnetic resonance sequence to guide ventricular tachycardia ablation in patients with cardiac defibrillators. *EP Europace.* 2020;22:598-606.
17. Hilbert S, Weber A, Nehrke K, et al. Artefact-free late gadolinium enhancement imaging in patients with implanted cardiac devices using a modified broadband sequence: Current strategies and results from a real-world patient cohort. *EP Europace.* 2017;20:801-807.
18. Detsky JS, Stainsby JA, Vijayaraghavan R, Graham JJ, Dick AJ, Wright GA. Inversion-recovery-prepared SSFP for cardiac-phase-resolved delayed-enhancement MRI. *Magn Reson Med*. 2007;58:365-372.
19. Zhang L, Lai P, Roifman IR, Pop M, Wright GA. Multi-contrast volumetric imaging with isotropic resolution for assessing infarct heterogeneity: Initial clinical experience. *NMR Biomed.* 2020;33:e4253.
20. Bhagirath P, Campos FO, Hopman L, et al. Impact of phase-correction of late-gadolinium enhancement images on quantification of scar metrics and in-silico VT-modelling in patients with an ischemic cardiomyopathy. *EP Europace*. 2024;26:euae102.309.
21. Detsky JS, Gideon P, Dick AJ, Wright GA. Reproducible classification of infarct heterogeneity using fuzzy clustering on multicontrast delayed enhancement magnetic resonance images. *IEEE Trans Med Imaging*. 2009;28:1606-1614.
22. Hong K, DiBella EV, Kholmovski EG, Ranjan R, McGann CJ, Kim D. Synthetic LGE derived from cardiac T1 mapping for simultaneous assessment of focal and diffuse cardiac fibrosis. *J Cardiovasc Magn Reson.* 2014;16:362.
23. Abdula G, Nickander J, Sorensson P, et al. Synthetic late gadolinium enhancement cardiac magnetic resonance for diagnosing myocardial scar. *Scand Cardiovasc J.* 2018;52:127-132.
24. Hong K, Jeong EK, Wall TS, Drakos SG, Kim D. Wideband arrhythmia-insensitive-rapid (AIR) pulse sequence for cardiac T1 mapping without image artifacts induced by an implantable-cardioverter-defibrillator. *Magn Reson Med.* 2015;74:336-345.
25. Shao J, Rashid S, Renella P, Nguyen KL, Hu P. Myocardial T1 mapping for patients with implanted cardiac devices using wideband inversion recovery spoiled gradient echo readout. *Magn Reson Med.* 2017;77:1495-1504.
26. Zhang L, Huttin O, Marie PY, et al. Myocardial infarct sizing by late gadolinium-enhanced MRI: Comparison of manual, full-width at half-maximum, and n-standard deviation methods. *J Magn Reson Imaging.* 2016;44:1206-1217.
27. Heiberg E, Engblom H, Carlsson M, et al. Infarct quantification with cardiovascular magnetic resonance using "standard deviation from remote" is unreliable: Validation in multi-centre multi-vendor data. *J Cardiovasc Magn Reson.* 2022;24:53.
28. Schmidt A, Azevedo CF, Cheng A, et al. Infarct tissue heterogeneity by magnetic resonance imaging identifies enhanced cardiac arrhythmia susceptibility in patients with left ventricular dysfunction. *Circulation.* 2007;115:2006-2014.
29. Lee S, Kim P, Im DJ, et al. The image quality and diagnostic accuracy of T1-mapping-based synthetic late gadolinium enhancement imaging: Comparison with conventional late gadolinium enhancement imaging in real-life clinical situation. *J Cardiovasc Magn Reson.* 2022;24:28.
30. Sheagren CD, Tran BTT, Patel JH, Lau AZ, Wright GAS. SyntheticLGE.Jl: An open-source toolbox for retrospective T1 fitting and synthetic LGE image generation. In: *Proceedings of the ISMRM 33rd Annual Meeting*. International Society of Magnetic Resonance in Medicine; 2024a.
31. Guo F, Krahn PRP, Escartin T, Roifman IR, Wright G. Cine and late gadolinium enhancement MRI registration and automated myocardial infarct heterogeneity quantification. *Magn Reson Med.* 2021;85:2842-2855.
32. Krumm P, Martirosian P, Brendel A, et al. T1 mapping MOLLI 5(3)3 acquisition scheme yields high accuracy in 1.5 T cardiac magnetic resonance. *Diagnostics.* 2022;12:2729.
33. Xue H, Shah S, Greiser A, et al. Motion correction for myocardial T1 mapping using image registration with synthetic image estimation. *Magn Reson Med.* 2012;67:1644-1655.
34. Yushkevich PA, Piven J, Hazlett HC, et al. User-guided 3D active contour segmentation of anatomical structures: Significantly improved efficiency and reliability. *Neuroimage.* 2006;31:1116-1128.

35. Warner J, Sexauer J, Unnikrishnan A, et al. JDWarner/scikit-fuzzy: Scikit-Fuzzy version 0.4.2. 2019.
36. Walt S, Schönberger JL, Juan N-I, et al. Scikit-image: Image processing in python. *PeerJ.* 2014;2:e453.
37. Wright G, Ospalak R, Sheagren C, et al. Wideband motion-corrected T1 mapping at 3 T: Evaluation in healthy volunteers. *J Cardiovasc Magn Reson.* 2024;26:926.
38. Kellman P, Larson AC, Hsu LY, et al. Motion-corrected free-breathing delayed enhancement imaging of myocardial infarction. *Magn Reson Med.* 2005;53:194-200.
39. Bhuva A, Ramlall M, Boubertakh R, et al. Wideband free breathing MOCO LGE changes patient care in patients with implantable cardiac defibrillators. *Heart.* 2017;103:A11-A12.
40. Orini M, Seraphim A, Graham A, et al. Detailed assessment of low-voltage zones localization by cardiac MRI in patients with implantable devices. *JACC: Clin. Electrophysiol.* 2022;8:225-235.
41. Sheagren CD, Cao T, Patel JH, et al. Motion-compensated T_1 mapping in cardiovascular magnetic resonance imaging: A technical review. *Front Cardiovasc Med.* 2023;10:1160183.
42. Guan X, Yang HJ, Zhang X, et al. Non-electrocardiogram-gated, free-breathing, off-resonance reduced, high-resolution, whole-heart myocardial T2* mapping at 3 T within 5 min. *Magn Reson Med.* 2024;91:1936-1950.
43. Zhao M, Shen D, Fan L, et al. Incorporation of view sharing and KWIC filtering into GRASP-pro improves spatial resolution of single-shot, multi-TI, late gadolinium enhancement MRI. *NMR Biomed.* 2024;37:e5059.
44. Sheagren CD, Kadota BT, Patel JH, Chiew M, Wright GA. Accelerated cardiac parametric mapping using deep learning-refined subspace models. In: Camara O, Puyol-Anton E, Sermesant M, et al., eds. *Statistical Atlases and Computational Models of the Heart. Regular and CMRxRecon Challenge Papers.* Lecture Notes in Computer Science. Springer Nature; 2024b:369-379.
45. Zhang L, Lai P, Pop M, Wright GA. Accelerated multicontrast volumetric imaging with isotropic resolution for improved peri-infarct characterization using parallel imaging, low-rank and spatially varying edge-preserving sparse modeling. *Magn Reson Med.* 2018;79:3018-3031.
46. Zhang Y, Zhao Y, Huang L, Xia L, Tao Q. Deep-learning-based roupwise registration for Motion correction of Cardiac mapping. In: Linguraru MG, Dou Q, Feragen A, et al., eds. *Medical Image Computing and Computer Assisted Intervention–MICCAI 2024.* Springer Nature; 2024:586-596.
47. Chow K, Flewitt JA, Green JD, Pagano JJ, Friedrich MG, Thompson RB. Saturation recovery single-shot acquisition (SASHA) for myocardial T1 mapping. *Magn Reson Med.* 2014;71:2082-2095.
48. Hamilton JI, Jiang Y, Chen Y, et al. MR fingerprinting for rapid quantification of myocardial T1, T2, and proton spin density. *Magn Reson Med.* 2017;77:1446-1458.
49. Guo F, Li M, Ng M, Wright G, Pop M. Cine and multicontrast late enhanced MRI registration for 3D heart model construction. In: Pop M, Sermesant M, Zhao J, et al., eds. *Statistical Atlases and Computational Models of the Heart. Atrial Segmentation and LV Quantification Challenges.* Springer International Publishing; 2019:49-57.
50. Popescu DM, Abramson HG, Yu R, et al. Anatomically informed deep learning on contrast-enhanced cardiac magnetic resonance imaging for scar segmentation and clinical feature extraction. *Cardiovasc Digit Health J.* 2022;3:2-13.
51. Bubenik P, Carlsson G, Kim PT, Luo Z. Statistical topology via Morse theory, persistence and nonparametric estimation. 2010.
52. Sheagren C, Escartin T, Krahn P, Patel J, Guo F, Wright G. Validation of automated topological LGE thresholding for Peri-infarct substrate characterization. In: *Proceedings of the Joint Annual Meeting ISMRM-ESMRMB ISMRT 31st Annual Meeting.* International Society of Magnetic Resonance in Medicine; 2022.

SUPPORTING INFORMATION

Additional supporting information may be found in the online version of the article at the publisher's website.

Figure S1. Choice of synthetic TI (TI_{syn}) affects tissue contrast and image quality, and must be performed separately for each subject. When the myocardial magnetization has not reached the nulling point (left two columns), the region of enhanced tissue is incorrect due to T1-dependent intensity shifts and the use of connected component filtering. After the myocardium has been successfully nulled, the enhanced tissue region is largely unaffected, but reduced contrast is seen between regions of healthy myocardium and scar. Threshold maps are depicted in the bottom row.

Figure S2. Effect of the cutoff probability GZ_{cut} on scarmaps compared to the reference LGE scarmaps. As GZ_{cut} increases, the gray zone volume decreases, but spatial localization of dense scar and gray zone is invariant under moderate shifts of GZ_{cut} from the value of 25% used for all analysis that visually aligns with the reference LGE.

Figure S3. Diagram of the 4(1)3(1)2 sequence used for post-Gd T_1 mapping for this sequence. Black indicates a wideband inversion pulse, and blue indicates the FLASH readout synchronized to cardiac diastole.

Table S1. Volumetric results for T_1^* mapping-based scarmaps with an ICD present and LGE scarmaps without an ICD present without the use of connected component filtering for any technique. Cluster: *Cluster-thresholding*; AC: *Artifact correction*; Union: *Dense scar union gray zone*.

How to cite this article: Sheagren CD, Escartin T, Patel JH, Barry J, Wright GA. Automated fibrosis segmentation from wideband post-contrast T_1^* mapping in an animal model of ischemic heart disease with implantable cardioverter-defibrillators. *Magn Reson Med*. 2025;93:2401-2413. doi: 10.1002/mrm.30468